



Fluid flow regime transition in water lubricated spiral grooved face seals

Noël Brunetière, Mathieu Rouillon

► To cite this version:

Noël Brunetière, Mathieu Rouillon. Fluid flow regime transition in water lubricated spiral grooved face seals. Tribology International, 2021, 153, pp.106605. 10.1016/j.triboint.2020.106605 . hal-03036808

HAL Id: hal-03036808

<https://hal.science/hal-03036808>

Submitted on 2 Dec 2020

HAL is a multi-disciplinary open access archive for the deposit and dissemination of scientific research documents, whether they are published or not. The documents may come from teaching and research institutions in France or abroad, or from public or private research centers.

L'archive ouverte pluridisciplinaire **HAL**, est destinée au dépôt et à la diffusion de documents scientifiques de niveau recherche, publiés ou non, émanant des établissements d'enseignement et de recherche français ou étrangers, des laboratoires publics ou privés.

Fluid flow regime transition in water lubricated spiral grooved face seals

Noël Brunetière^{a,*}, Mathieu Rouillon^b

^a*Institut Pprime, CNRS- Université de Poitiers - Ensma, 86360 Chasseneuil du Poitou, France*

^b*Pags Robotics, 39170 Coteaux du Lizon, France*

Abstract

Spiral grooves are used to enhance the generation of a fluid film between the sliding surfaces of a mechanical face seal when fluids with poor lubrication properties are to be sealed. This technical solution allows reducing asperity contact, wear, and friction during operation, due to the full film between the surfaces. However because of the thickness of the film, the fluid flow regime can turn from laminar to turbulent. This transition can significantly affect the performance of the seal and needs to be evaluated. Simulations have been performed of a water lubricated seal with spiral grooves. The numerical model solves the Reynolds equation and the energy equation in the fluid film. The thermo-mechanical fluid–solid coupling is considered. The theoretical predictions of the temperature are compared with experimental findings obtained on a dedicated test rig with face seals of different groove depths. This comparison [allows](#) to identify the critical Reynolds numbers corresponding to a transition of the fluid flow regime.

Keywords: Hydrodynamic lubrication, Transition, Turbulence, Mechanical Seal, Spiral grooves

*Corresponding author

Email addresses: noel.brunetiere@univ-poitiers.fr (Noël Brunetière), mathieu.rouillon@pagesgroup.net (Mathieu Rouillon)

1. Introduction

Mechanical face seals are sealing devices used in many rotating machines, such as pumps, agitators, and compressors. They are basically composed of two flat annular rings, one linked to the shaft and the other to the housing. Their
5 good operation is possible due to the lubrication of the interface by the sealed fluid [1]. The fluid pressure in the interface is governed by the famous Reynolds equation [2]. One of the main assumptions used by Reynolds in 1886 to derive this equation is that the [flow](#) is laminar. For that he stated that the number defined as the product of the channel width, h , by the density of the fluid, ρ ,
10 the sliding speed V , and divided by the viscosity μ must be lower than 1400. The value of this number $Re = \frac{\rho V h}{\mu}$, known as the Reynolds number, must correspond to a laminar flow regime.

Generally speaking, the channel width or film thickness, h , in a mechanical seal is very small, lower than a micron [1], ensuring a laminar flow rate in the
15 interface. However, there are many situations where a lack of contact between the faces of the seal is needed, leading to a thicker film [3]. In these situations, non-laminar flows can occur.

The first example is the hydrostatic seal used in a reactor coolant pump in a nuclear power station. These seals are machined with a coning angle to
20 ensure a film wider than 10 microns. When combined with the high fluid flow experienced in the interface of such seals, it is possible to have a turbulent flow regime between the seal faces [4, 5, 6, 7]. This generally leads to a decrease in the flow rate compared to the laminar solution [4, 6], but some significant variations can be observed in the transition between laminar and turbulent flow
25 regimes [5, 7].

High film thickness can also be achieved in mechanical seals by means of hydrodynamic grooves, such as spiral grooves [8]. When this type of seal is used with low viscosity fluids, such as liquid oxygen [9] or water [\[10, 11, 12\]](#), non-laminar flow regimes can occur. As in hydrostatic seals, the appearance of
30 turbulence leads to a lower leakage rate [11]. In addition, the rate of increase of

the temperature in the contact is also affected by the flow regime [11].

Because turbulent flow regimes can occur not only in seals but in many other lubricated contacts, the development of a turbulence model for lubrication was initiated more than sixty years ago by Constantinescu [13], based on the concept
35 of the Prandtl mixing length. A few years later, an approach based on the law of Wall and the turbulent viscosity was proposed by Ng [14]. This model was then linearized to be applied to bearings [15]. An improvement was proposed to consider the central area of the flow by Elrod and Ng [16]. The consideration of surface roughness was added to the model more recently [7]. Another approach
40 based on a friction factor was proposed by Hirs [17].

There are thus some models for both laminar and turbulent flows. However the description of the transition regime is not so well understood and described. One usual method is to scale the turbulent viscosity by a scaling factor which gradually varies from 0 to 1 when the Reynolds number of the flow increases
45 [18]. When flow factors are used, a polynomial transition function can be used [19]. These approaches assume that the critical Reynolds number values at the transition are known. The first critical Reynolds number Re_ℓ corresponds to the end of the laminar flow regime and the second one Re_t corresponds to the beginning of the turbulent flow regime.

50 In the literature on mechanical seals, these critical numbers vary from one author to another. According to Lin and Yao [20], $Re_t = 1000$ whereas Brunetière et al. [6] assumed that $Re_\ell = 900$ and $Re_t = 1600$. Later, Brunetière [21] considered that $Re_\ell = 900$ and $Re_t = 1360$, in line with the experimental work of Bottin et al. on plane Couette flow [22]. In a recent paper, the authors [11]
55 found that a transition occurs at an average Reynolds number of 1500 without any distinction between Re_ℓ and Re_t . In the case of thrust bearings, Dousti and Allaire [23] used smaller values, $Re_\ell = 500$ and $Re_t = 800$. However, the transition in rotor stator disk systems is not as simple [24]. In the 60's, Daily and Neece studied the friction between a rotating disk enclosed in a chamber
60 [25]. They identified four different friction regimes, depending on the Reynolds number and the aspect ratio of the system $G = \frac{h}{R_o}$ where R_o is the outer radius

of the disk. Different transition mechanisms are observed with typical networks of vortices [26]. The transition corresponding to lower values of G was experimentally and numerically studied by Sankov and Smirnov [27, 28]. They show
65 a strong dependence of the critical Reynolds number Re_ℓ on the value of G . However, their study was limited to values of G higher than 10^{-2} , whereas in mechanical seals, this number can be two orders of magnitude lower. Some experimental works on thrust bearings were presented at the Leeds Lyon symposium in 1975 by Gregory [29] and Frêne [30] at slightly lower values of G . In
70 2004, Harada and Tuskasazaki [31] presented a thorough experimental study of a thrust-bearing-like configuration where they identified the critical Reynolds numbers for a larger range of G , down to 2×10^{-3} . This value is, however, much larger than in mechanical seals.

In the present paper, experimental results obtained for a spiral grooved face
75 seal lubricated in water and working in laminar and turbulent flow regimes are used to identify the critical Reynolds number at values of G typical of mechanical seals. To obtain the local values of the parameters in the interface and obtain the critical values, a numerical model is also used. The results are also compared to critical values from the literature.

80 2. Materials and methods

2.1. Mechanical seals

A view of the spiral grooved face seal used in this study is presented in Figure 1. The main characteristics of the seal are presented in Table 1. Compared to the one used in a previous paper [11], where only a groove depth of $h_g = 10\mu\text{m}$
85 was used, here two additional values of h_g (5 and 20) are tested. Since the thickness of the film is mainly controlled by the groove depth, this allows varying significantly the Reynolds number during the tests. Note that the real value of the groove depths was measured with a white light interferometer (Talysurf CCI 6000). The measured values are given between brackets in Table 1. These
90 measured values were used for all the computations presented in the paper.

The rotor is made of silicon carbide (SiC) and the stator is made of carbon graphite (C). Their main physical properties can be found in Table 2.

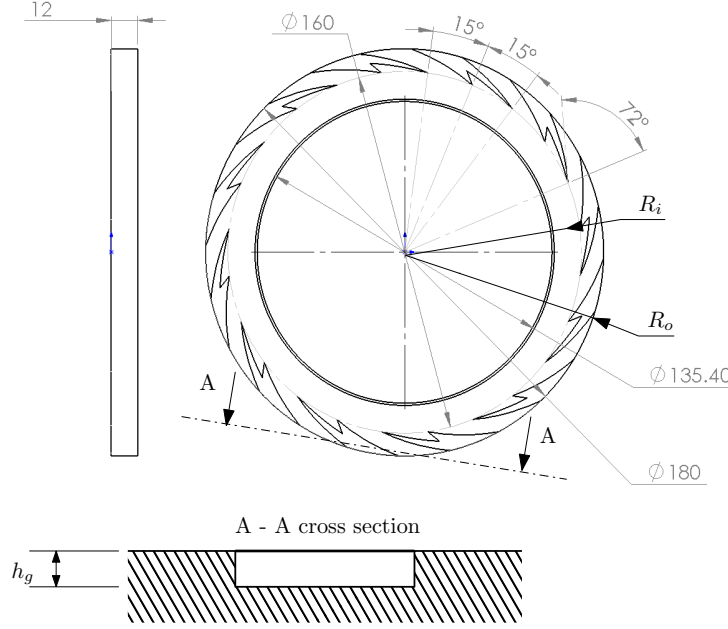


Figure 1: View of the rotating ring of the spiral grooved seal

2.2. Test rig

A cross-sectional view of the experimental cell is presented in Figure 2. Two
 95 mechanical seals are placed back to back to suppress the axial force due to fluid
 pressure. The test cell is fed by water from the bottom pipe. The water is
 provided by an hydraulic equipment at a flow rate of 30 l/min and a controlled
 temperature up to 95 °C and a pressure up to 5 MPa. The shaft is driven by an
 hydrostatic spindle to ensure accurate motion and rotated by an electric motor
 100 up to 6000 rpm. The operating conditions are given in Table 3.

2.3. Measurements and test procedure

During the tests, the operating conditions (pressure, temperature, and flow
 rate of the water, rotation speed) were controlled and measured. The leakage

Table 1: Main characteristics of the mechanical seal

Parameter	Value
Outer radius R_o	90 mm
Inner radius R_i	70 mm
Balance ratio B	0.827
Groove depth h_g	5 (5.9), 10 (10.3), 20 (21.1) μm
Number of grooves	12
Rotor material	Silicon carbide
Stator material	Carbon graphite
Balance ratio	0.827
Spring force	97.1 N

Table 2: Seal faces materials

Parameter	Stator	Rotor
Material	Carbon graphite	Silicon carbide
Thermal conductivity k ($\text{W.m}^{-1}.\text{K}^{-1}$)	7.96	148.8
Density ρ (kg.m^{-3})	1680	3100
Young's modulus E (GPa)	13.79	413.7
Poisson's ratio	0.2	0.2
Coefficient of expansion λ ($10^{-6}.\text{K}^{-1}$)	4.9	4.1

Table 3: Operating conditions of the mechanical seal

Parameter	Value
Fluid	Water
Temperature T_f	40 °C to 95 °C
Pressure P_o	1 to 5 MPa
Rotation speed ω	2000 to 6000 rpm
Flow rate	30 l/min

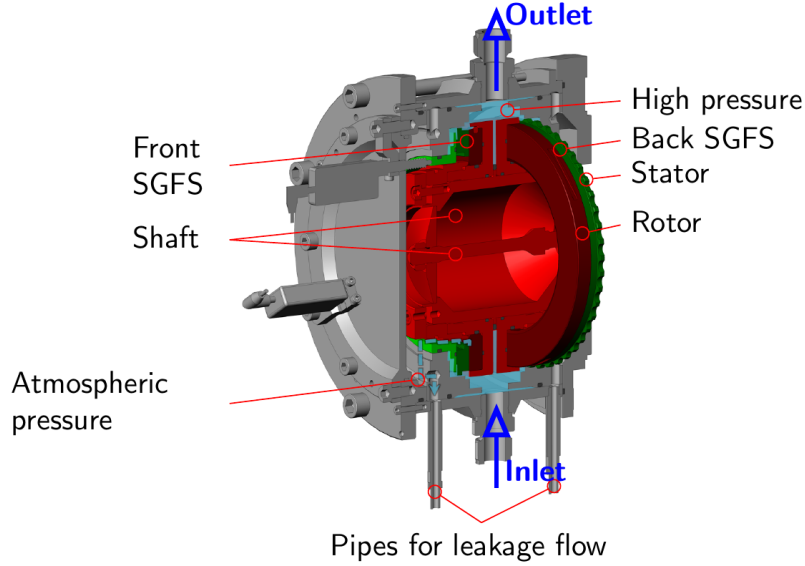


Figure 2: Cross section of the experimental cell

of the seals was collected by dedicated pipes (see Figure 2) and driven to a
 105 weighing cell (BJ6100d) to be measured as a function of time. The test cell
 was mounted on an hydrostatic bearing to allow friction torque measurement
 in the mechanical seals. A calibration was carried out to remove the effects of
 the different pipes on the measured torque. Two thermocouples (type T) were
 stuck within the stator of the front mechanical seal. The one located at $r = 76.3$
 110 mm and 1 mm below the surface will be used in the present paper.

For each test, after specifying the operating conditions, and after the torque,
 leakage rate and temperature had stabilized, the values provided by the sensors
 were recorded for a period of 40 s. An average over this period was then taken.
 Each test was repeated three times. Individual experimental point presented in
 115 the following sections corresponds to the average of these three tests. The error
 bar indicates the maximum and minimum values among the three tests.

2.4. Numerical model

2.4.1. Turbulence model

The turbulence model is based on the turbulent viscosity approach proposed
 120 by Ng, Elrod and Pan [14, 15, 16] and modified by Brunetière and Tournier
 [7]. The eddy viscosity is expressed by

$$\frac{\epsilon_M}{\nu} = 0.4 \left(z^+ \bar{\tau} - 10.7 \tanh \frac{z^+ \bar{\tau}}{10.7} \right) \quad (1)$$

where $z^+ = z \sqrt{\frac{\rho}{\tau_w}}$ is the dimensionless distance to the wall, ν is the kinematic
 viscosity of the fluid, ρ is the fluid density, τ_w is the wall shear stress, and
 $\bar{\tau} = |\frac{\tau}{\tau_w}|$ is the dimensionless local shear stress. The apparent viscosity is, thus,

$$\mu_a = \mu \left(1 + \delta_\epsilon \frac{\epsilon_M}{\nu} \right) \quad (2)$$

125 where δ_ϵ is the scaling factor introduced to deal with the transition to turbulence.

In line with the paper of Brunetière [21], it is defined by

$$\begin{cases} \delta_\epsilon = 0 & Re \leq Re_\ell \\ 0 < \delta_\epsilon < 1 & Re_\ell < Re < Re_t \\ \delta_\epsilon = 1 & Re_t \leq Re \end{cases} \quad (3)$$

to ensure that the turbulent viscosity vanishes in the laminar flow regime and
 is fully considered in the turbulent regime. In the transition, the following
 variation is used [21]:

$$\delta_\epsilon = 0.5 \left\{ 1 - \cos \left[\pi \left(\frac{Re_t - Re}{Re_t - Re_\ell} \right)^{0.6} \right] \right\} \quad (4)$$

130 The values of Re_ℓ and Re_t will be determined by means of a comparison with
 the experimental results.

2.4.2. Flow model

The usual viscous thin film assumptions are used to derived the flow model.
 The flow rates per unit length in the x and y direction are thus

$$q_x = V_x \frac{I_1}{I_0} \rho h + \frac{\rho h^3}{\mu} \left(I_2 - \frac{I_1^2}{I_0} \right) \times \left(\frac{\rho \omega^2 x}{3} - \frac{\partial p}{\partial x} \right) \quad (5)$$

$$q_y = V_y \frac{I_1}{I_0} \rho h + \frac{\rho h^3}{\mu} \left(I_2 - \frac{I_1^2}{I_0} \right) \times \left(\frac{\rho \omega^2 x}{3} - \frac{\partial p}{\partial y} \right) \quad (6)$$

135 where $V_x = -y\omega$ and $V_y = x\omega$ are the wall velocity, and ω is the rotor angular velocity. These equations consider the centrifugal force induced by the seal rotation on the flows. The I_n terms are integrals over the film thickness considering the apparent viscosity variations:

$$I_n = \frac{1}{h^{n+1}} \int_0^h \frac{z^n}{\mu_a} dz \quad (7)$$

The mass conservation equation is

$$\frac{\partial q_x}{\partial x} + \frac{\partial q_y}{\partial y} = 0. \quad (8)$$

140 By developing this equation, the Reynolds equation is recovered.

The energy conservation in the fluid film is expressed with the enthalpy H of the fluid:

$$q_x \frac{\partial H}{\partial x} + q_y \frac{\partial H}{\partial y} = q_s - V_x \tau_{xz} - V_y \tau_{xy} \quad (9)$$

where q_s is the heat flux to the contiguous solids (the rotor and stator). This equation can be applied to two-phase flows, unlike the energy equation expressed
145 with the temperature. Indeed, the pressure and temperature are not independent parameters in the two-phase region. In the case of two phases, the fluid is assumed to be a homogeneous mixture of liquid and vapor. The studied fluid is water and its properties are based on the IAPWS formulations [32].

2.4.3. Fluid–solids coupling

150 The two solids are assumed to be axisymmetrical. Thus the pressure and heat flux are circumferentially averaged and then applied to the solid surfaces. The heat flux q_s is related to the temperature T_s of the surface of the solid and the fluid temperature T by mean of a convection law [33]:

$$q_s = -\frac{k}{h} \left(\frac{C_p \mu}{k} \right)^{1/3} (T - T_s) \quad (10)$$

where C_p is the thermal capacity of the fluid and k its thermal conduction coefficient.

In addition, the position of the stator and thus the average film thickness is adjusted to ensure a force balance between the fluid force in the film and the closing force.

2.4.4. Boundary conditions and numerical method

The pressure is imposed at the inner and outer radii of the sealing interface. The enthalpy is imposed at nodes where an inlet flow occurs. Indeed, because of the grooves, a reverse flow can occur. Because the energy equation 9 is a first order partial differential equation, no boundary condition is needed at the outlet. The boundary conditions for the seal rings are presented in Figure 3.

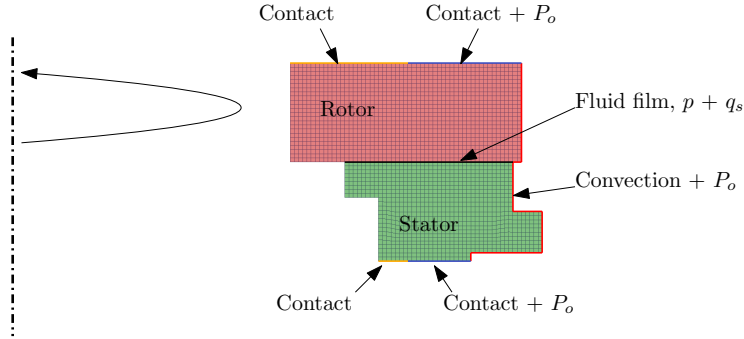


Figure 3: Boundary conditions of the seal rings

The Reynolds equation 8 and the energy equation 9 are solved using the finite element method as described in [34, 35]. The heat transfer and deformation are also calculated using the finite element method. Some iteration loops are necessary to ensure force balance and energy balance.

3. Results

3.1. Examples of numerical results in extreme conditions

The first simulation results presented in Figure 4 were obtained at low fluid temperature and with low groove depth ($T_f = 40$ °C and $h_g = 5.9$ μm). The flow regime is assumed to be laminar and the extreme values of the Reynolds number in the fluid film are 725 and 1500. As discussed in the next sections, these values indeed correspond to a laminar flow regime. One can see the pressure spikes generated in the grooves, leading to additional hydrodynamic forces maintaining a full film between the faces. The minimum film thickness is 8.1 μm . A temperature rise of about 16 K is reached in the solid. Note that the groove depth is not exactly the theoretical value, but it is based on the values actually measured on the seal rings. Moreover, because of meshing limits in the simulation code, the groove shape is slightly simplified. It is assumed that this does not change the results.

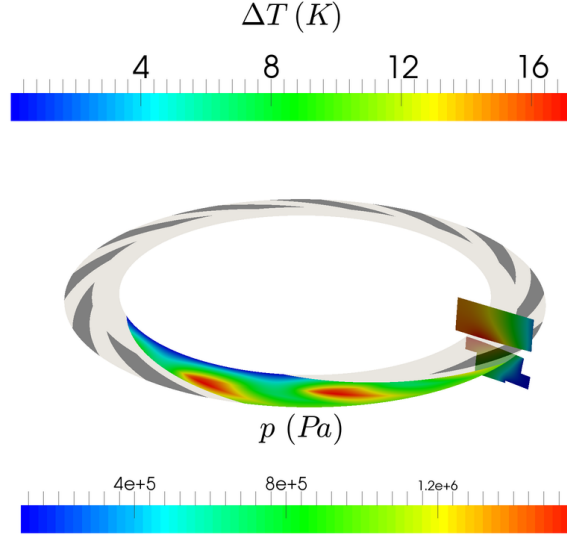


Figure 4: Pressure distribution in the fluid film and temperature rise in seal rings at $\omega = 6000$ rpm, $P_o = 1$ MPa, $T_f = 40$ °C and with groove depth $h_g = 5.9$ μm

The first simulation results presented in Figure 5 were obtained at high

fluid temperature and with high groove depth ($T_f = 95$ °C and $h_g = 21.1$ μm)
 185 and assuming a turbulent flow regime. The minimum and maximum Reynolds
 numbers in the liquid film are 2000 and 6500, confirming the assumptions of the
 calculation. That these are higher than in the previous case are due to the fact
 that the film is thicker (the minimum film thickness is 12.8 μm) and has a lower
 viscosity (0.25 mPa.s compared 0.48 mPa.s in the first simulation). Because of
 190 these differences, the pressure spikes in the grooves are of lower magnitude, as is
 the temperature rise in the solids. In addition, a partial phase change is observed
 in this case at the inner radius where the fluid is exiting the sealing interface.
 The temperature at this location is limited to the saturation temperature, which
 is close to 100 °C at atmospheric pressure. The temperature rise is thus limited
 195 to 5 K at the inner radius, which is materialized by a slight cooling of the solid
 at the fluid outlet location.

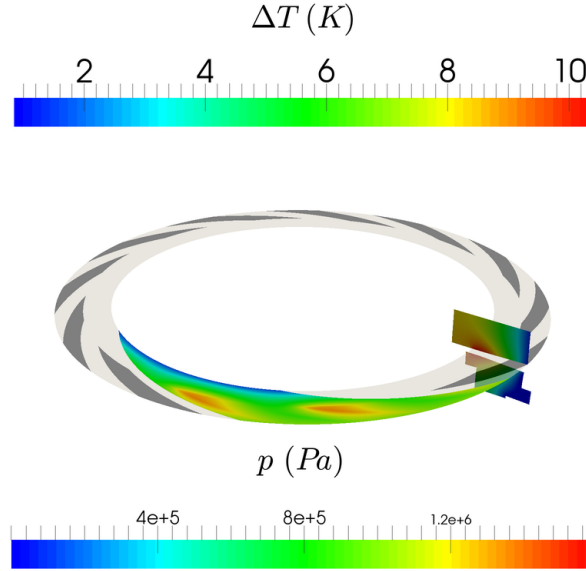


Figure 5: Pressure distribution in the fluid film and temperature rise in seal rings at $\omega = 6000$ rpm, $P_o = 1$ MPa, $T_f = 95$ °C and with groove depth $h_g = 21.1$ μm

3.2. Experimental results

In this section, the temperature rise measured in the stator is presented, for different operating conditions. This parameter is used because it exhibits
 200 a more evident dependence on the flow regime than do the leakage rate or the friction torque. However, the friction torque and leakage measurements are used in the next sections.

The first set of results presented in Figure 6 were obtained at the lowest rotation speed (2000 rpm). The temperature rise in the stator is presented as
 205 a function of the temperature of the sealed fluid, for the three different groove depth values. As expected when the fluid temperature is increased, the fluid viscosity is reduced, leading to a decrease in viscous dissipation and a rise in the temperature. The same result is obtained when the groove depth, and thus the film thickness, is increased. Even though the temperature rise is small (lower
 210 than 3 K), a monotonic trend of the curves is observed.

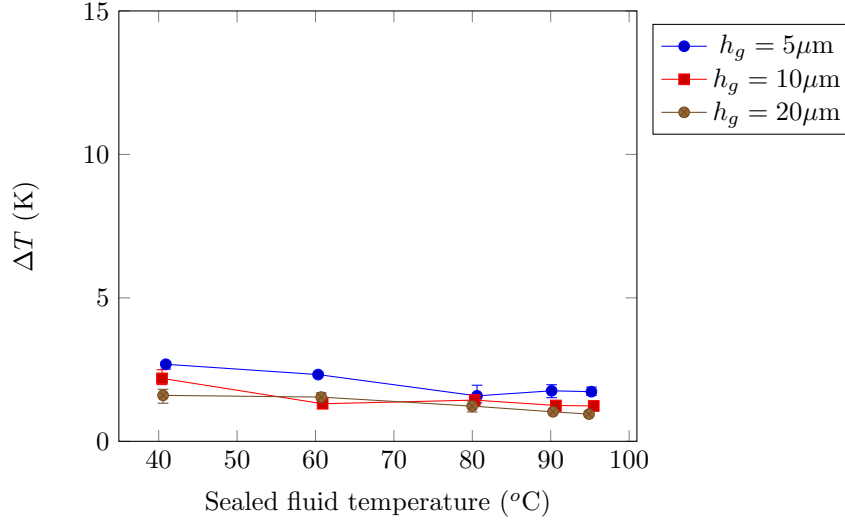


Figure 6: Temperature rise in the stator as a function of the sealed fluid temperature for $\omega = 2000$ rpm and $P_o = 1$ MPa

When the rotating speed is raised to 6000 rpm, the results are different (Figure 7). First of all, the average temperature rise is obviously significantly

higher (about 10 K). Even if the monotonic decreasing trend is almost preserved when the groove depth is 5 μm , this is no longer the case when h_g is increased
215 to 10 or 20 μm . Indeed, an increase of several K in the temperature rise in the stator can be measured when the sealed fluid temperature is increased from 40 $^{\circ}\text{C}$ to 60 $^{\circ}\text{C}$ for $h_g = 20 \mu\text{m}$ and from 60 $^{\circ}\text{C}$ to 80 $^{\circ}\text{C}$ for $h_g = 10 \mu\text{m}$. It has been shown with the numerical simulation that the fluid flow regime can change from laminar to turbulent in these conditions. This change can explain the
220 non-monotonic evolution of the temperature as observed by Gregory in thrust bearings [29].

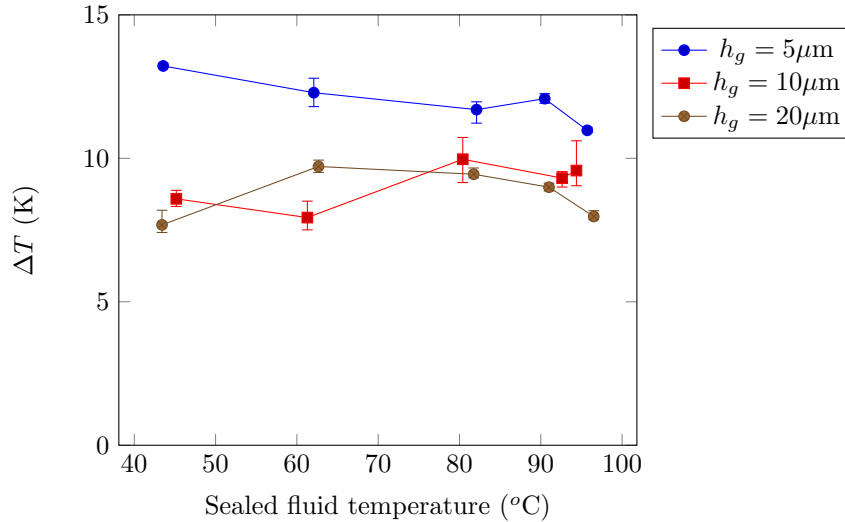


Figure 7: Temperature rise in the stator as a function of the sealed fluid temperature for $\omega = 6000 \text{ rpm}$ and $p_o = 1 \text{ MPa}$

3.3. Determination of the critical Reynolds numbers

The experimental results presented in Figure 7 are reproduced by simulation assuming a laminar flow regime and a turbulent flow regime. The comparison
225 of experiments and numerical simulations is presented in Figures 8 to 10 for $h_g = 5$ to 20 μm . When the flow is assumed to be laminar, the obvious results are obtained: the temperature rise in the stator decreases when the sealed fluid

or the groove depth are increased. The same conclusion can be reached for the turbulent flow regime. However, for each groove depth, the temperature rise is much higher (about two times the laminar value) when the flow regime is turbulent. This is not surprising since turbulence leads to an increase in the apparent viscosity of a fluid (see Equations 1 and 2). The experimental temperature rise is also shown in Figures 8 to 10. It can be seen that the values are not aligned with either the laminar simulation curves or turbulent simulation curves. The measured values are close to the laminar simulated values at low temperatures of the sealed fluid and tend to the turbulent simulated values when the temperature of the sealed fluid is increased. Moreover the distance from the turbulent solution is reduced when the groove depth is increased.

Based on this, it is possible to identify one point, P_ℓ , for $h_g = 5.9 \mu\text{m}$ where the flow regime is at the limit of the laminar regime and one point, P_t for $h_g = 21.1 \mu\text{m}$ where the flow regime is at the limit of the turbulent regime. These points are shown in Figures 8 and 10. Using the corresponding simulation results, it is possible to find the critical Reynolds numbers:

$$Re_\ell = \max [Re (P_\ell)] = 1500 \quad (11)$$

$$Re_t = \min [Re (P_t)] = 1660 \quad (12)$$

Using these critical values, it has been possible to run simulations using the transition model described by Equations 3 and 4. The results are presented in Figures 8 to 10 with a bold line. The obtained results are in better correlation with the experiments. More particularly, when $h_g = 20 \mu\text{m}$, the results are in excellent agreement. For the other depth values, the agreement is not so good, but the general experimental non-monotonic trends are captured by the model, which is not the case when fully laminar or fully turbulent descriptions are used.

4. Discussion

It is shown in the literature that the critical Reynolds numbers characterizing the end of the laminar flow regime, Re_ℓ , and the beginning of the turbulent flow

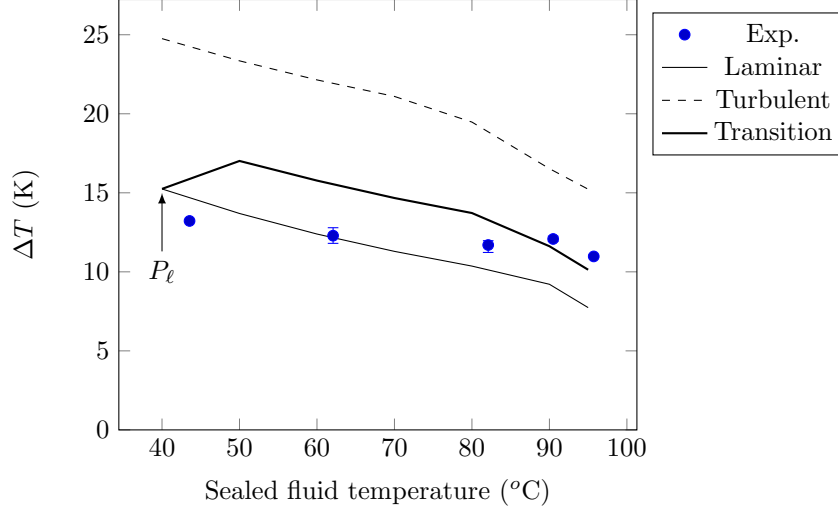


Figure 8: Temperature rise in the stator as a function of the sealed fluid temperature for $\omega = 6000$ rpm and $P_o = 1$ MPa with $h_g = 5.9 \mu\text{m}$

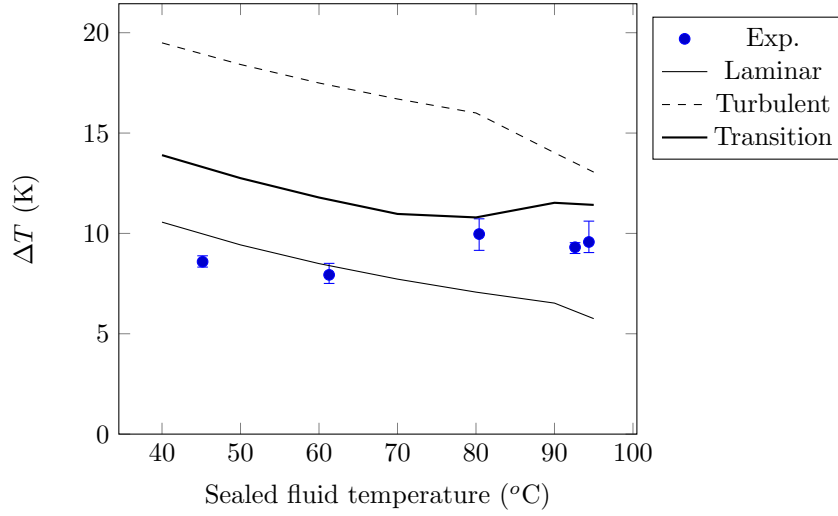


Figure 9: Temperature rise in the stator as a function of the sealed fluid temperature for $\omega = 6000$ rpm and $P_o = 1$ MPa with $h_g = 10.3 \mu\text{m}$

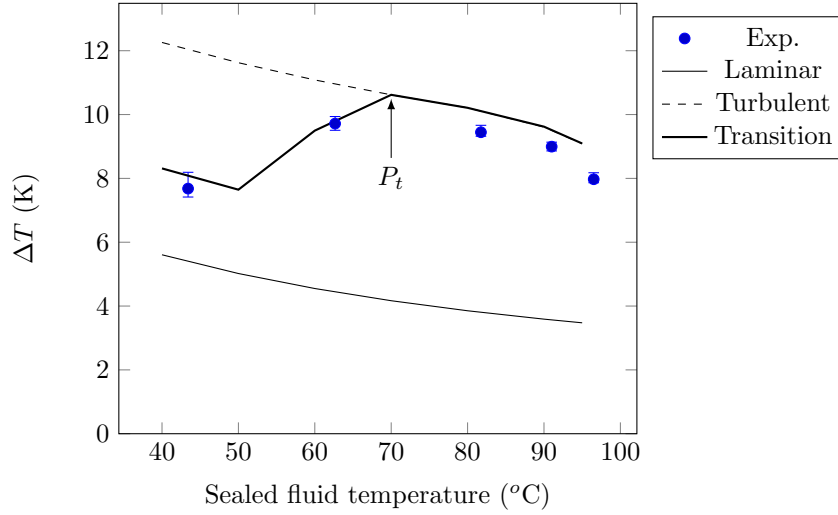


Figure 10: Temperature rise in the stator as a function of the sealed fluid temperature for $\omega = 6000$ rpm and $P_o = 1$ MPa with $h_g = 21.1\mu\text{m}$

regime, Re_t , depend on the aspect ratio $G = \frac{h}{R}$, where h is the distance between
the rotor and the stator and R is the radius of the rotor. The results cited in
the Introduction are reported in Figure 11 as well as the values calculated in the
previous section. The stability analysis carried out by San'kov and Smirnov [28]
to determine Re_ℓ is in agreement with the experimental data when $G < 5 \times 10^{-3}$.
They show that Re_ℓ increases when the gap ratio is decreased. The experimental
data of Harada and Tsukazaki [31] highlight a stabilization of Re_ℓ to a value
of about 1200 when G is between 2 and 5×10^{-3} . The global trend of Re_t is
to decrease toward Re_ℓ when G is decreased. However no values are available
for lower values of G . The critical values calculated in the present paper were
obtained for values of G of about 2×10^{-4} , that is to say, one order of magnitude
lower than those investigated by Harada and Tsukazaki. Additional results in
the interval between 2×10^{-4} to 2×10^{-3} would be necessary to check the
consistency of our results with the literature.

Even if the simulation results were satisfactory compared to the experimental
results in Figures 8 to 10, it would be interesting to check the consistency of the

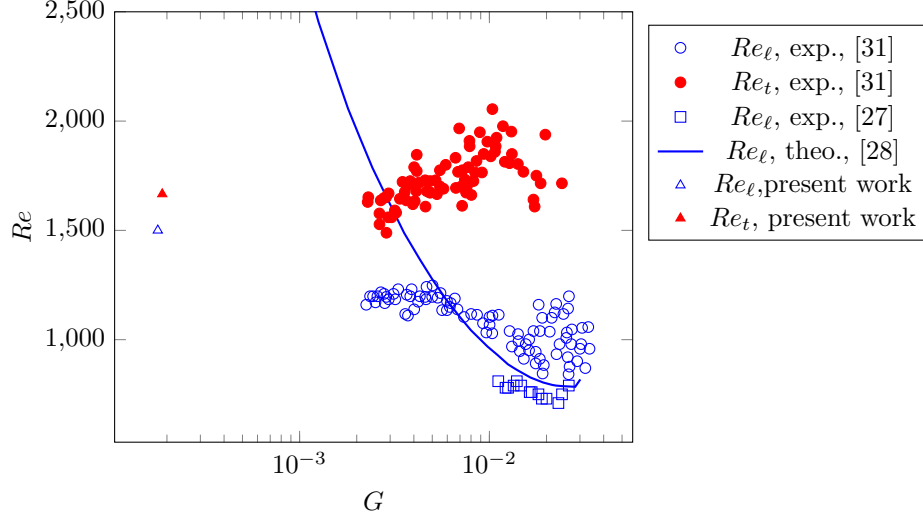


Figure 11: Critical Reynolds numbers as a function of the aspect ratio $G = \frac{h}{R_o}$, comparison to literature data

critical Reynolds number found with all the experimental results. For that, it is necessary to calculate the Reynolds number of the fluid flow during the tests. The film thickness was, however, not measured, and a theoretical derivation of the film thickness is necessary.

Using the numerical model, it was possible to show that friction coefficients can be scaled for all the values of the groove depths when using the following dimensionless number:

$$G^* = \frac{\mu\omega(R_o + R_i)(R_o - R_i)^3}{2F_c h_g^2} = G' \times \frac{(R_o - R_i)^2}{h_g^2} \quad (13)$$

where F_c is the closing force applied to the seal and G' the usual duty parameter.

$$f^* = \frac{2C_f(R_o - R_i)}{F_c(R_o + R_i)h_g} = f \times \frac{R_o - R_i}{h_g} \quad (14)$$

where C_f is the friction torque and f the apparent friction coefficient.

All the experimental values of f^* are presented as a function of G^* in Figure 12. The experimental values obtained with the three groove depths and different operating conditions are superimposed and well fitted by the theoretical

black line. This line was obtained with the numerical model assuming a laminar isothermal flow with rigid walls. It can be seen that just a few points, corresponding to a possible turbulent regime and a two-phase flow, are not aligned with the other results.

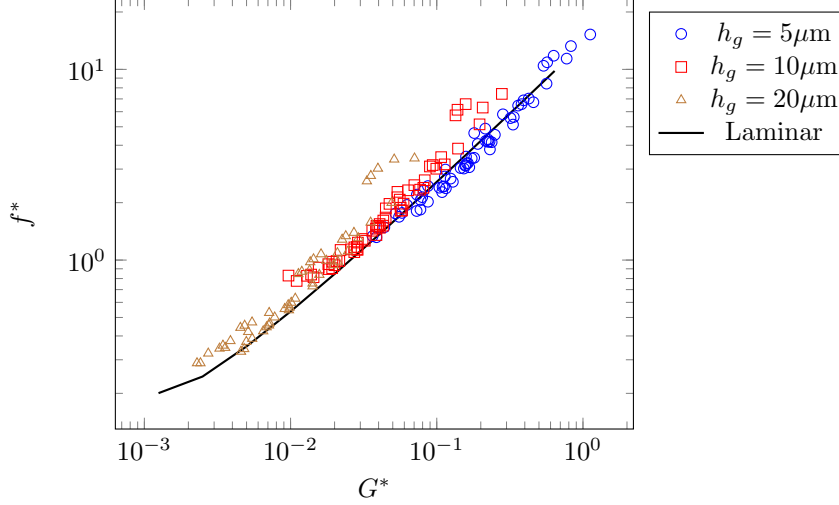


Figure 12: Modified friction coefficient as a function of the modified duty parameter

Using the numerical simulation, it was possible to fit the film thickness as a function of the modified duty parameter:

$$\frac{h}{h_g} \simeq 1.95 (G^*)^{0.37} \quad (15)$$

The film thickness Equation 15 can be applied to all the experimental data to have an estimate of the film thickness and then compute the Reynolds number of the flow.

Daily and Neece [25] show that the changes in the flow regime can be identified by means of the torque coefficient C_m :

$$C_m = \frac{4C_f}{\rho\omega R_o} \quad (16)$$

The torque coefficient was calculated for each experimental case and is presented as a function of the Reynolds number $Re = \frac{\rho\omega R_o h}{\mu}$ in Figure 13. This coefficient was computed with the numerical model assuming a fully laminar flow

regime (solid line), fully turbulent flow regime (dashed line), and the transition approach (thick solid line). At low Reynolds numbers, the experimental data are in good agreement with the laminar solution, which exhibits a slope of -1, typical of the laminar regime [25]. When the Reynolds number is higher than about 1000, a deviation toward the turbulent line is observed, for both experiments and simulation. The experimental points are not perfectly superimposed in the transition region. One reason is that the Reynolds number is calculated using an estimate of the film thickness assuming a laminar flow regime (Equation 15). Secondly, as can be seen with the simulation results, the transition occurs in two phases. The first one corresponds to the change of the regime in the grooves and then a regime transition in the dam. The relative position of the two phases depends on the ratio of the film width to the groove depth. The simulation was done for $h_g = 10 \mu\text{m}$. Even if the correlation is not perfect, the model is consistent with the measurements. In addition, a slope of -0.25 is reached at high Reynolds numbers typical of turbulent friction in small gaps [25].

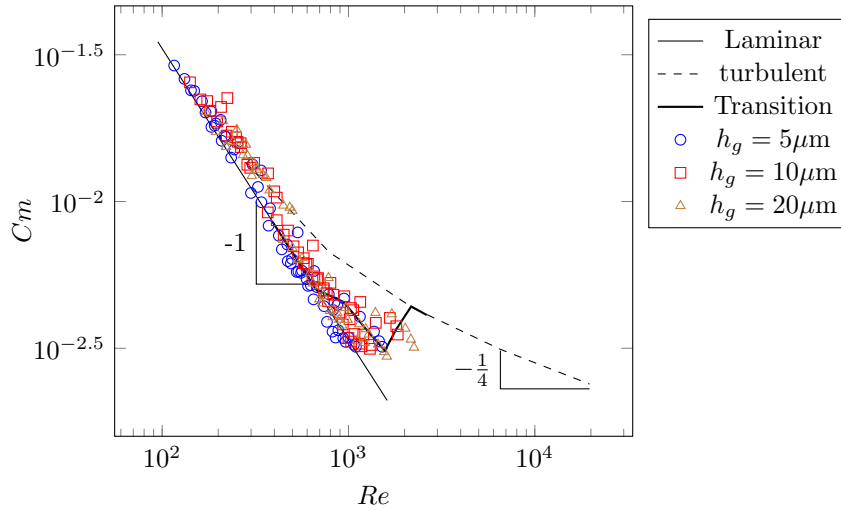


Figure 13: Friction factor as a function of the Reynolds number based on the calculated film thickness

In a previous paper [11], the authors showed that the flow regime can be

identified with the thermal growth rate. Let us define a dimensionless thermal growth rate:

$$T^* = \frac{\Delta T h_{av}}{\mu \omega^2 R_o^3 k} \quad (17)$$

315 where k is the stator thermal conductivity (see Table 2). h_{av} is calculated using Equation 15 and assuming that h_g covers 25 % of the sealing area, thus $h_{av} = h + 0.25h_g$. T^* is the dimensionless ratio of the temperature rise to the power dissipated by viscous friction. It is expected that because of the increase of the apparent viscosity when the flow regime turns from laminar to turbulent, 320 a slope change is visible when T^* is presented as a function of the Reynolds number. Two Reynolds numbers are considered: the minimum and maximum Reynolds numbers in the film. They are calculated using respectively the inner radius and the film thickness and the outer radius and the film plus the groove depth.

325 T^* is presented as a function of the maximum Reynolds number in Figure 14. If this number is lower than $Re_\ell = 1500$, the fluid flow regime is laminar. This limit is shown in the figure. Generally speaking, T^* is a decreasing function of the maximum Reynolds number until the end of the laminar flow regime. Beyond this number, T^* tends to increase. It is correlated with the 330 rapid increase in the apparent viscosity in the transitional regime.

Then T^* is plotted as a function of the minimum Reynolds number in Figure 15. The flow is fully turbulent when the minimum Reynolds number is higher than $Re_t = 1660$. This limit is indicated in the figure. It can be seen that only a few cases operate in the fully turbulent flow regime. In addition, the increase 335 of T^* in the transition regime to turbulence can be clearly seen in the figure.

In these two figures, the experimental points are not aligned because T^* is affected by a number of physical phenomena not considered in the Reynolds number: variation of viscosity with the local temperature, deformation of the seal rings, cooling of the rings varying with the rotation speed. However, some 340 clear tendencies confirm that the flow regime changes are well captured with

the critical values of the Reynolds number identified in the results section.

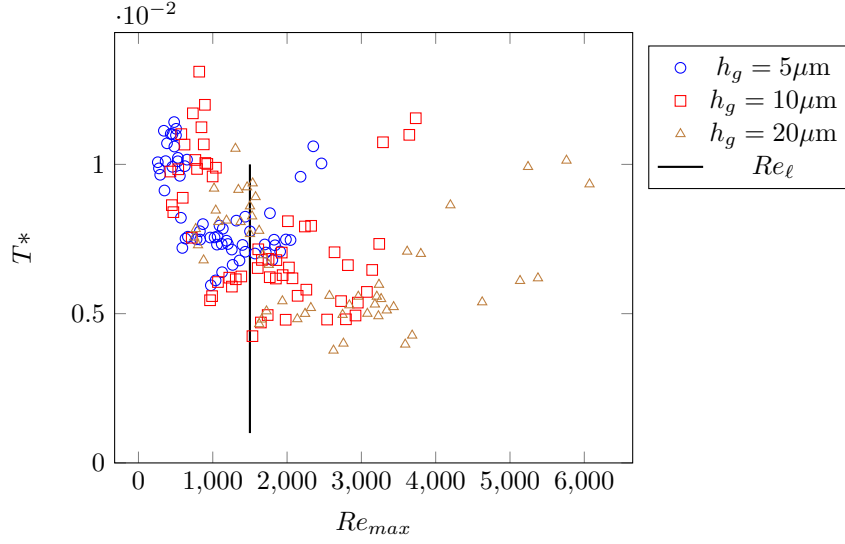


Figure 14: Growth rate of dimensionless temperature as a function of the maximum Reynolds number

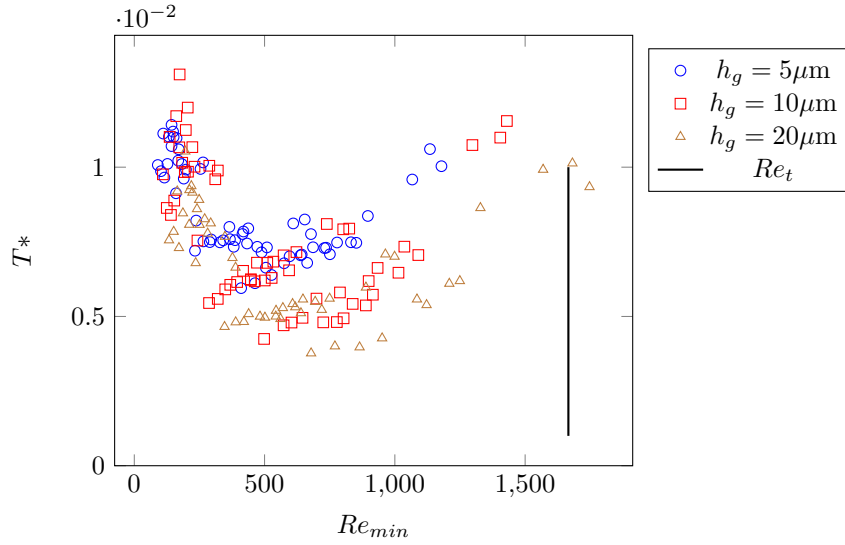


Figure 15: Growth rate of dimensionless temperature as a function of the minimum Reynolds number

5. Conclusion

Water lubricated spiral grooved face seals can work at high Reynolds numbers where the flow regime is no longer laminar. By comparing numerical and experimental results for the temperature, it was possible to identify the critical Reynolds number corresponding to the end of the laminar flow regime ($Re_\ell = 1500$) and the critical Reynolds number corresponding to the beginning of the turbulent flow ($Re_t = 1660$). These number were obtained for very low values of the gap ratio $G \sim 2 \times 10^{-4}$, typical of mechanical seals. This gap ratio is ten times lower than values available in the literature. It is of importance since the critical Reynolds numbers are dependent on the gap ratio. The consistency of the results was demonstrated using the friction and temperature results of a large number of experiments.

Acknowledgments

We thank the CNES and Ariane Group for the PhD opportunity, their scientific investment in the project, and their financial support. This work was partially presented and published at the BHR Group 24th International Conference on Fluid Sealing, 7-8 March 2018, Manchester. BHR Group is thanked for allowing the authors to publish this work in Tribology International. This work pertains to the French government program Investissements dAvenir (LABEX INTERACTIFS, reference ANR-11-LABX-0017-01).

References

- [1] A. Lebeck, Principle and Design of Mechanical Face Seals, John Wiley & Sons, Inc., New York, 1991.
- [2] O. Reynolds, On the theory of lubrication and its application to mr. beauchamp tower's experiments, including an experimental determination of the viscosity of olive oil, Philosophical Transactions of the Royal Society

of London 177 (1886) 157–234.

URL <https://doi.org/10.1098/rstl.1886.0005>

- 370 [3] T. Lai, J. Netzel, A review of non-contacting face seals, in: Q. Wang, J. Netzel, F. Sadeghi (Eds.), Proceedings of the 1999 STLE / ASME H.S. Cheng Tribology Surveillance - The advancing Frontier of Engineering Tribology, 1999, pp. 131–139.

- 375 [4] T. Koga, T. Fujita, The hydrostatic noncontact seal including fluid inertia effect, ASLE Transactions 29 (1) (1986) 35–42.

URL <https://doi.org/10.1080/05698198608981657>

- [5] N. Brunetière, B. Tournier, J. Frêne, Influence of fluid flow regime on performances of non-contacting liquid face seals, Journal of Tribology 124 (3) (2002) 515–523.

380 URL <https://doi-org.ressources.univ-poitiers.fr/10.1115/1.3159386>

- [6] N. Brunetière, E. Galenne, B. Tournier, I. Pierre-Danos, Modelling of non laminar phenomena in high reliability hydrostatic seals operating in extreme conditions, Tribology International 41 (4) (2008) 211–220.

385 URL <https://doi.org/10.1016/j.triboint.2007.07.002>

- [7] N. Brunetière, B. Tournier, Study of hydrostatic mechanical face seals operating in turbulent rough flow regime, Journal of Tribology 131 (3) (2009) 032202.

390 URL <https://doi-org.ressources.univ-poitiers.fr/10.1115/1.3139051>

- [8] T. Lai, Development of non-contacting, non-leaking spiral groove liquid face seals, Lubrication Engineering 50 (8) (1994) 625–631.

- [9] W. Shapiro, J. Walowit, H. F. Jones, Analysis of spiral-groove face seals for liquid oxygen, A S L E Transactions 27 (3) (1984) 177–188.

395 URL <https://doi.org/10.1080/05698198408981559>

- [10] G.-Y. Zhang, W.-G. Zhao, X.-T. Yan, X.-Y. Yuan, A theoretical and experimental study on characteristics of water-lubricated double spiral grooved seals, *Tribology Transactions* 54 (3) (2011) 362–369.
URL <https://doi.org/10.1080/10402004.2010.546035>
- 400 [11] M. Rouillon, N. Brunetière, Spiral groove face seal behavior and performance in liquid lubricated applications, *Tribology Transactions* 61 (6) (2018) 1048–1056.
URL <https://doi.org/10.1080/10402004.2018.1463426>
- [12] S. Zhang, S. Jiang, X. Lin, Static and dynamic characteristics of high-speed water-lubricated spiral-groove thrust bearing considering cavitating
405 and centrifugal effects, *Tribology International* 145 (2020) 106159.
URL <https://doi.org/10.1016/j.triboint.2020.106159>
- [13] V. N. Constantinescu, On turbulent lubrication, *Proceedings of the Institution of Mechanical Engineers* 173 (1) (1959) 881–900.
410 URL https://doi.org/10.1243/PIME_PROC_1959_173_068_02
- [14] C. Ng, Fluid dynamic foundation of turbulent lubrication theory, *ASLE Transactions* 7 (1964) 311–321.
URL <https://doi.org/10.1080/05698196408972061>
- [15] C. Ng, C. Pan, A linearized turbulent lubrication theory, *Journal of Basic Engineering* 87 (1965) 675–688.
415 URL <https://doi-org.ressources.univ-poitiers.fr/10.1115/1.3650640>
- [16] H. Elrod, C. Ng, A theory for turbulent films and its application to bearings, *Journal of Lubrication Technology* 89 (3) (1967) 346–362.
420 URL <https://doi-org.ressources.univ-poitiers.fr/10.1115/1.3616989>
- [17] G. Hirs, Bulk flow theory for turbulence in lubricant films, *Journal of Lubrication Technology* 95 (2) (1973) 137–146.

- URL <https://doi-org.ressources.univ-poitiers.fr/10.1115/1.3451752>
- 425
- [18] A. Z. Szeri, Fluid Film Lubrication, 2nd Edition, Cambridge University Press, 2010.
URL <https://doi.org/10.1017/CB09780511782022>
- [19] N. Zirkelback, L. San Andr  s, Bulk flow model for the transition to turbulence regime in annular pressure seals, Tribology Transactions 39 (4) (1996) 835–842.
430
URL <https://doi.org/10.1080/10402009608983602>
- [20] J. Lin, C. Yao, Hydrodynamic lubrication of face seal in a turbulent flow regime, Journal of Tribology 118 (3) (1996) 589–600.
435
URL <https://doi.org/10.1115/1.2831578>
- [21] N. Brunet  re, A modified turbulence model for low reynolds number - application to hydrostatic seals, Journal of Tribology 127 (1) (2005) 130–140.
URL <https://doi-org.ressources.univ-poitiers.fr/10.1115/1.1829721>
440
- [22] S. Bottin, O. Dauchot, F. Daviaud, Intermittency in a locally forced plane couette flow, Physical Review Letters 79 (22) (1997) 4377–4380.
URL http://prola.aps.org/abstract/PRL/v79/i22/p4377_1
- [23] S. Dousti, P. Allaire, A thermohydrodynamic approach for single-film and double-film floating disk fixed thrust bearings verified with experiment, Tribology International 140 (2019) 105858.
445
URL <https://doi.org/10.1016/j.triboint.2019.105858>
- [24] J. Owen, R. Rogers, Flow and Heat Transfer in Rotating Disc Systems, Vol.1: Rotor-Stator Systems, Research Studies Press, Taunton, U. K., 1989.
- [25] J. Daily, R. Nece, Chamber dimension effects on induced flow and frictional resistance of enclosed rotating disks, Journal of Basic Engineering 82
450

(1960) 217–232.

URL <https://doi-org.ressources.univ-poitiers.fr/10.1115/1.3662532>

- 455 [26] L. Schouveiler, P. Le Gal, M. Chauve, Instabilities of the flow between a rotating and a stationary disk, *Journal of Fluid Mechanics* 443 Schouveiler 2001 (2001) 329–350.

URL <https://doi-org.ressources.univ-poitiers.fr/10.1017/S0022112001005328>

- 460 [27] P. San'kov, E. Smirnov, Bifurcation and transition to turbulence in the gap between rotating and stationary parallel disks, *Fluid Dynamics* 19 (5) (1984) 695–702.

URL <https://doi-org.ressources.univ-poitiers.fr/10.1007/BF01093534>

- 465 [28] P. San'kov, E. Smirnov, Stability of viscous flow between rotating and stationary disks, *Fluid Dynamics* 26 (6) (1991) 857–864.

URL <https://doi-org.ressources.univ-poitiers.fr/10.1007/BF01056787>

- [29] R. Gregory, Operating characteristics of a fluid-film thrust bearing subjected to high shaft speeds, in: D. Dowson, M. Godet, C. Taylor (Eds.), *Proceedings of the 2nd Leeds Lyon Symposium*, MEP, London, Insa de Lyon, 1975, pp. 154–162.

- [30] J. Frêne, Discussion on session viii - general contribution, in: D. Dowson, M. Godet, C. Taylor (Eds.), *Proceedings of the 2nd Leeds Lyon Symposium*, MEP, London, Insa de Lyon, 1975, pp. 166–167.

- 475 [31] M. Harada, J. Tsukazaki, On the transition from laminar to turbulence in the fluid film of thrust bearings, in: *14th International Colloquium Tribology*, Vol. II, TAE, 2004, pp. 1025–1030.

- [32] W. Wagner, A. Pru, The iapws formulation 1995 for the thermodynamic
 480 properties of ordinary water substance for general and scientific use, Journal
 of Physical and Chemical Reference Data 31 (2) (2002) 387–535.
 URL <https://doi.org/10.1063/1.1461829>
- [33] L. San Andres, T. Kim, Thermohydrodynamic analysis of bump type gas
 foil bearings: A model anchored to test data., ASME. J. Eng. Gas Turbines
 485 Power. 132 (4) (2012) 042504–042504–10.
 URL <https://doi.org/10.1115/1.3159386>
- [34] N. Brunetiere, Modelling of reverse flows in a mechanical seal, Tribology
 Online 11 (2016) 94–101.
 URL <https://doi.org/10.2474/trol.11.94>
- 490 [35] N. Brunetiere, A general model for liquid and gas lubrication, including
 cavitation, Journal of Tribology 140 (2018) 021702–10p.
 URL <https://doi.org/10.1115/1.4037355>
- [36] S. Candel, Fluid Mechanics (in French), Paris, 1996.

Appendix

495 The enthalpy H equation for the energy conservation equation [36] with the
 thin film assumptions can be written :

$$\rho v_x \frac{\partial H}{\partial x} + \rho v_y \frac{\partial H}{\partial y} + \rho v_z \frac{\partial H}{\partial z} = -\frac{\partial q}{\partial z} + \tau_{xz} \frac{\partial v_x}{\partial z} + \tau_{yz} \frac{\partial v_y}{\partial z} + v_x \frac{\partial p}{\partial x} + v_y \frac{\partial p}{\partial y} \quad (18)$$

where v_x , v_y and v_z are the components of the fluid velocity. The momentum
 equations for a thin fluid film are:

$$\frac{\partial p}{\partial x} = \frac{\partial \tau_{xz}}{\partial z} \quad (19)$$

$$\frac{\partial p}{\partial y} = \frac{\partial \tau_{yz}}{\partial z} \quad (20)$$

Using these results, the energy equation can simplified:

$$\rho v_x \frac{\partial H}{\partial x} + \rho v_y \frac{\partial H}{\partial y} + \rho v_z \frac{\partial H}{\partial z} = -\frac{\partial q}{\partial z} + \frac{\partial \tau_{xz} v_x}{\partial z} + \frac{\partial \tau_{yz} v_y}{\partial z} \quad (21)$$

500 This equation is then integrated in through film direction z from 0 to h . In addition it is assumed that:

$$H \simeq \frac{1}{h} \int_0^h H dz \quad (22)$$

The integrated energy equation is:

$$\frac{\partial H}{\partial x} \int_0^h \rho v_x dz + \frac{\partial H}{\partial y} = - \int_0^h \frac{\partial q}{\partial z} dz + \int_0^h \frac{\partial \tau_{xz} v_x}{\partial x} dz + \int_0^h \frac{\partial \tau_{yz} v_y}{\partial y} dz \quad (23)$$

It can be written:

$$q_x \frac{\partial H}{\partial x} + q_y \frac{\partial H}{\partial y} = q_s - V_x \tau_x - V_y \tau_y \quad (24)$$

where q_s is the heat flux to the contiguous solids (the rotor and stator), V_x and
 505 V_y are the rotor velocity components and τ_x and τ_y the shear stress on the rotor surface.